ACS Sustainable Chemistry & Engineering

Research Article

Cite This: ACS Sustainable Chem. Eng. 2018, 6, 16121−16129

pubs.acs.org/journal/ascecg

Na-Rich Prussian White Cathodes for Long-Life Sodium-Ion Batteries

Zhilong Shen,[†] Songhao Guo,[‡] Chunli Liu,[†] Yunpo Sun,[†] Zhen Chen,[§] Jian Tu,[§] Shuangyu Liu,[∥] Jipeng Cheng,[†] Jian Xie,*[,†,⊥] Gaoshao Cao,[⊥] and Xinbing Zhao[†,⊥]

[†]State Key Laboratory of Silicon Materials, School of Materials Science and Engineering, Zhejiang University, Zheda Road #38, Hangzhou 310027, China

[‡]Center for High Pressure Science and Technology Advanced Research (HPSTAR), Cailun Road 1690#, Shanghai 201203, China

[§]LI-FUN Technology Corporation Limited, Chuangye Road #128, Zhuzhou 412000, China

[∥]State Key Laboratory of Advanced Transmission Technology, Global Energy Interconnection Research Institute Co. Ltd., Binhe Road#18, Beijing 102211, China

[⊥]Key Laboratory of Advanced Materials and Applications for Batteries of Zhejiang Province, Zheda Road #38, Hangzhou 310027, China

Supporting Information

ABSTRACT: Prussian blue analogues (PBA) recently have received great interest for promising applications in low-cost sodium-ion batteries (SIBs). However, controlled synthesis of high-performance PBA is still challenging. In this work, a facile precipitation route was used to synthesize Na-rich PBAs with superior electrochemical performance. It was found that two shapes of the products, namely, small irregular particles and large cuboid particles, coexist by adding sodium citrate in the sodium hexacyanoferrate side during the synthesis. The product shows large capacity (144 mAh g^{-1} under a 0.1 C rate), good rate performance (115.6 mAh g^{-1} under a 1 C rate, 86.6 mAh g^{-1} under a 10 C rate), and long-term cycling stability (73.4% retention after 780 cycles under a 0.5 C rate, 72.7% retention after 2100 cycles under a 1 C rate). This work offers a promising route to prepare PBA-based cathode materials for high-performance SIBs.

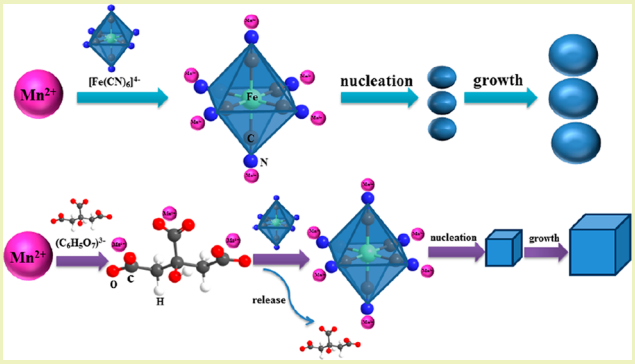

KEYWORDS: *Prussian blue analogue, Sodium-ion battery, Cathode material, Sodium manganese hexacyanoferrate, Electrochemical performance*

INTRODUCTION

The rapid consumption of lithium in Li-ion batteries (LIBs) causes a worldwide concern on lithium resources due to the limited reserves and uneven global distribution.[1] Therefore, considerable attention has been paid to alternatives to LIBs, such as those based on Na^+, K^+, Mg^{2+}, and Al^{3+} ions.[2−4] Among these, sodium-ion batteries (SIBs) have attained a special interest owing to abundant Na resources and a similar working mechanism as LIBs.[5−12] Despite recent advances, some critical obstacles need to be overcome for the practical uses of SIBs, one of which is to develop suitable cathode materials.[13−17] Previous reports showed that some potential SIBs cathodes, such as $NaFePO_4$,[18] $NaNi_{1/3}Co_{1/3}Mn_{1/3}O_2$,[19] and $NaMn_2O_4$,[20] are electrochemically inactive or inert with lower capacity or voltage compared with their LIBs analogues. The relatively larger radius of Na ions and other related factors are considered to underlie the difference in crystal structure and electrochemical properties.[7] In comparison, Prussian blue analogues (PBAs) hold great promise due to the unique open frameworks with large channels for Na-ion transportation.[21−31]

As Na-storage hosts, PBAs-based materials have a general structural formula of $Na_xM_2[M_1(CN)_6]_y{\cdot}nH_2O$ ($0 \le x \le 2, 0 \le y \le 1$), where M_1 and M_2 are the elements of transitional metals.[32] Usually, M_1 is Fe and M_2 is Fe, Mn, or Co since Fe^{2+}/Fe^{3+}, Mn^{2+}/Mn^{3+}, and Co^{2+}/Co^{3+} redox couples contribute to the capacity.[33−35] PBAs are usually synthesized in aqueous phase at low temperature. The resulting products usually have lower Na content than expected due to the presence of interstitial water and lattice defects in PBAs crystals, which limits their yieldable capacity.[21,32] Besides, PBAs exhibit a poor electronic conductivity, leading to poor rate performance. To enhance the electrochemical properties of PBAs, a lot of measures were taken, including removal of interstitial water,[36] lattice doping,[37] forming hybrids with conducting materials,[25,38,39] synthesizing Na-rich phase under optimized conditions,[24] and generating unique morpholo-

Received: June 12, 2018
Revised: October 25, 2018
Published: November 4, 2018

DOI: 10.1021/acssuschemeng.8b02758
ACS Sustainable Chem. Eng. 2018, 6, 16121−16129

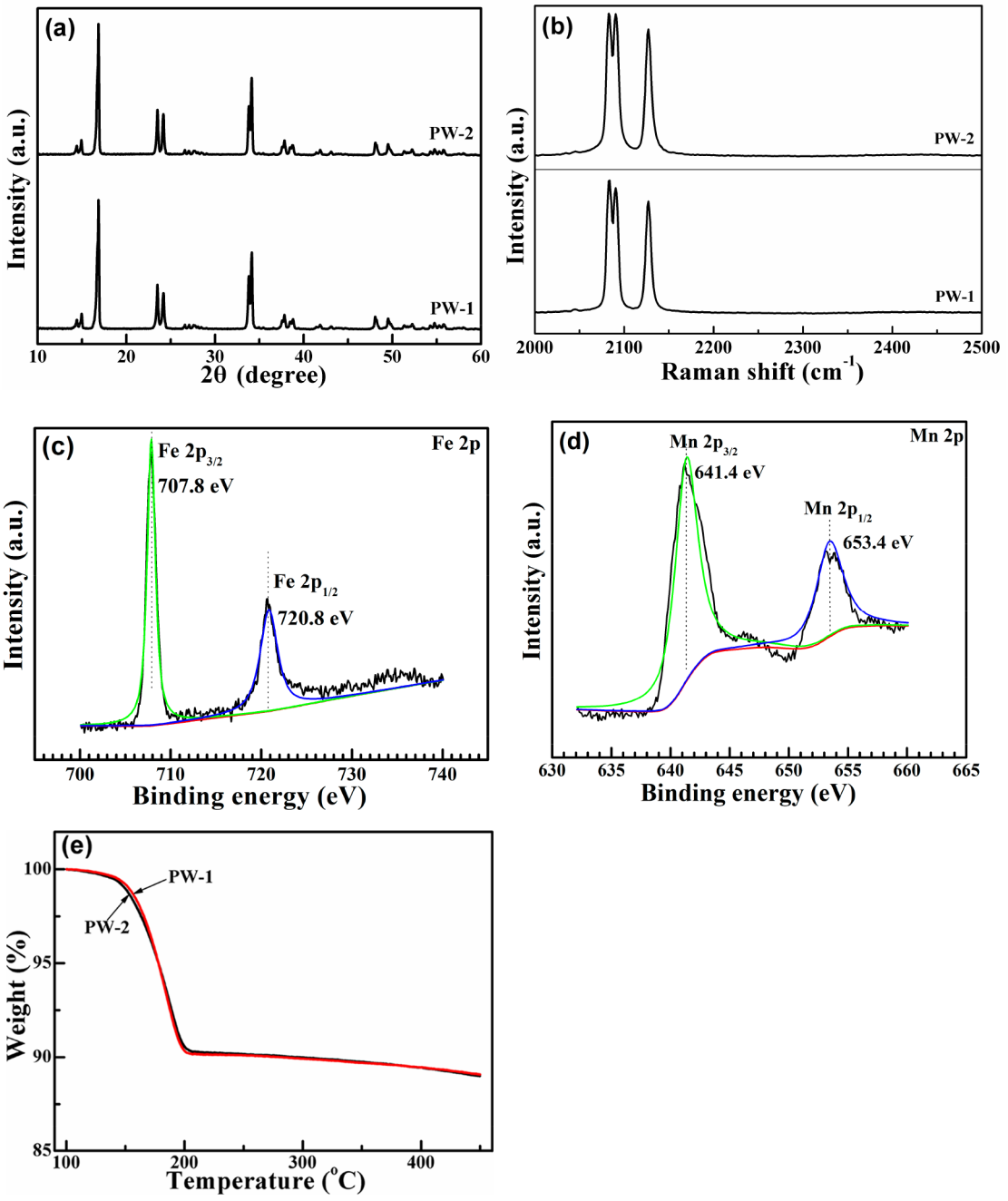

Figure 1. (a) XRD patterns PW-1 and PW-2, (b) Raman spectra of PW-1 and PW-2, (c) Fe 2p and (d) Mn 2p XPS of PW-1, and (e) TG of PW-1 and PW-2.

gies.[40] The Guo group reported that the PBA/carbon nanotubes (CNT) composite exhibited a long life and outstanding rate performance even at low temperature.[39] The work reported by Huang et al. demonstrated that, through inhibitor and temperature control, border-rich PBAs could be produced with high capacity and superior cycling stability.[40]

In this work, sodium manganese hexacyanoferrate ($Na_xMnFe(CN)_6$) was prepared by a precipitation method. Compared with $Na_xFeFe(CN)_6$, $Na_xMnFe(CN)_6$ is more promising since it has a higher working voltage.[32] It was found that a Na-rich monoclinic phase $Na_xMnFe(CN)_6$ was obtained by performing the precipitation reaction at high temperature and adding sodium citrate in the precursor solution. The Na-rich product is white colored (Prussia white) and is composed of small irregular particles in submicron scale and large cuboid particles in micron scale. The $Na_xMnFe(CN)_6$ prepared by this route shows a large capacity, good rate performance, and long-term cycling stability, showing promising applications in high-performance SIBs.

EXPERIMENTAL SECTION

Starting Materials. Sodium hexacyanoferrate ($Na_4Fe(CN)_6 \cdot 10H_2O$, ≥ 99% purity) and manganese sulfate monohydrate ($MnSO_4 \cdot H_2O$, ≥ 99% purity) were purchased from Sigma-Aldrich. Sodium chloride (NaCl, 99.5% purity) and sodium citrate dihydrate ($Na_3C_6H_5O_7 \cdot 2H_2O$, 99% purity) were purchased from Sinopharm Chemical Reagent Co., Ltd.

DOI: 10.1021/acssuschemeng.8b02758
ACS Sustainable Chem. Eng. 2018, 6, 16121−16129

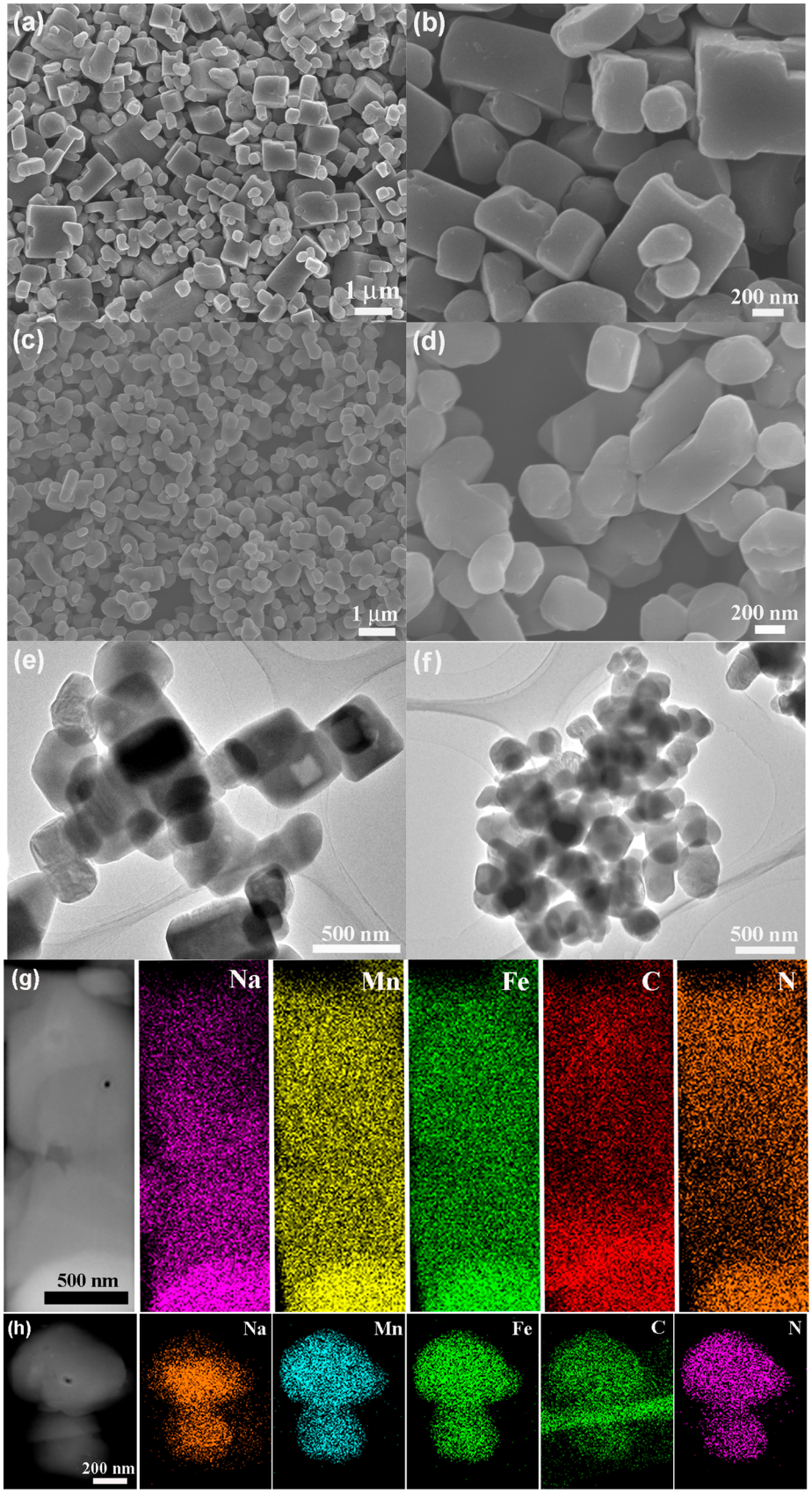

Figure 2. SEM images of (a,b) PW-1 and (c,d) PW-2, TEM image of (e) PW-1 and (f) PW-2, and HAADF-STEM images and EDX mapping of (g) cuboid and (h) irregular particles.

DOI: 10.1021/acssuschemeng.8b02758
ACS Sustainable Chem. Eng. 2018, 6, 16121−16129

Materials Preparation. Prussia white (PW) materials were synthesized using a coprecipitation route. Sodium hexacyanoferrate (3 mmol), sodium citrate (12 mmol), and sodium chloride (0.24 mol) were dissolved in deionized (DI) water (100 mL) with strong stirring. The above solution was poured into a 1 L flask after complete dissolution of the reactants. The flask with the solution was then heated to 85 °C with N_2 flowed in. $MnSO_4{\cdot}H_2O$ (6 mmol) was dissolved in DI water (100 mL) with magnetic stirring to form the $MnSO_4$ solution, followed by dropwise adding into the flask using a peristaltic pump (1 mL min^{-1}) to form a white suspension. The white suspension was aged for 3 h under continuous stirring at 85 °C. The white precipitate was then separated by centrifugation followed by washing with DI water sufficiently. After that, the sample was vacuum-dried for 18 h at 110 °C. The obtained PW was named PW-1. For comparison, another two PW samples were synthesized using a similar method without adding sodium citrate in $Na_4Fe(CN)_6$ solution (PW-2) or adding sodium citrate in $MnSO_4$ solution (PW-3).

Materials Characterization. The phases in the obtained products were identified by X-ray diffraction (XRD). The XRD pattern was acquired on a Rigaku D/Max-2550pc diffractometer using Cu K_α radiation with a wavelength of 1.541 Å. The XRD pattern was refined with the Rietveld method using GSAS software. Scanning electron microscopy (SEM) was used to observe morphologies of the PW samples. The SEM observation was conducted on S-4800 field-emission microscope (Hitachi, Japan). The microstructure of the PW samples was characterized by transmission electron microscopy (TEM) and high-angle annular dark field-scanning transmission electron microscopy (HAADF-STEM). The TEM and HAADF-STEM characterizations were carried out using a FEI Titan G2 80-200 ChemiSTEM microscope. The applied acceleration voltage is 200 kV. The microstructure of the PW samples was further characterized by Raman spectroscopy using a DXR532 Raman imaging system (Thermo Fisher Scientific, U.S.A.). The measurements were performed using Ar-ion laser with a wavelength of 532 nm at a 10 mW power. X-ray photoelectron spectroscopy (XPS) was measured using a KRATOS AXIS ULTRA-DLD system (Shimadzu, Japan) with Al Kα radiation ($h\nu$ = 1486.6 eV). Thermogravimetric (TG) analysis was performed to determine the water content in the PW samples. The measurement was conducted on a Netzsch LFA467 instrument (NETZSCH, Germany) in N_2. The content of sodium, iron, and manganese was analyzed by inductively coupled plasma-atomic emission spectrometry (ICP-AES) using IRIS Intrepid II XSP system. C and N contents were measured using a Flash EA 1110 instrument.

Electrochemical Measurements. The slurry for electrode fabrication was prepared by mixing PW, Ketjen black, and polyvinylidene fluoride with a 7:2:1 mass ratio in *N*-methyl pyrrolidone with magnetic stirring. The electrode slurry was then pasted on Al foil to make the cathodes. Before cells fabrication, the electrodes were dried under vacuum overnight at 80 °C. The areal loading of PW on Al foils is about 2 mg cm^{-2}. Coin-type cells were fabricated in a glovebox filled with argon with metallic sodium as the anode. The separator used is Whatman GF glass fiber film. The electrolyte used is 1 mol L^{-1} $NaPF_6$ dissolved in a mixed solvent of diethyl carbonate (DEC)/ethylene carbonate (EC) in a volumetric ratio of 1:1. Fluoroethylene carbonate (FEC) was added to the electrolyte with a 5% volumetric ratio. Electrochemical properties of PW were tested by constant charge/discharge cycling using a Neware battery testing system (Neware Technology Limited, China) at 2.0–4.0 V (vs Na/Na^+). Cyclic voltammetry (CV) was performed using a VersaSTAT3 electrochemistry workstation (Princeton Applied Research) at 2–4.2 V vs Na/Na^+ with a scanning rate of 0.1 mV s^{-1}. Electrochemical impedance spectroscopy (EIS) was measured on the electrochemistry workstation by using a 10 mV AC voltage and a 10^{-2}–10^5 Hz frequency range. All of the electrochemical tests were conducted at room temperature.

RESULTS AND DISCUSSION

As shown in Figure 1a, both the products obtained at 85 °C have a monoclinic structure with a space group of $P2_1/n$.[22,41] Rietveld refinement analysis on the XRD patterns validates the monoclinic structure of the products (Figure S1). The parameters of the crystal lattice are determined to be a = 10.6461 Å, b = 7.5653 Å, c = 7.3536 Å, and β = 92.2010° by Rietveld refinement analysis, which agrees with the previous report.[36] As previously reported, the PBA with a monoclinic phase has a high Na content and thus a high capacity.[42] In comparison, the monoclinic structure of the product prepared at room temperature is not well developed (Supporting Information (SI), Figure S2a). Raman spectra of PW-1 and PW-2 are presented in Figure 1b, where three strong peaks are evident, which are all related to $(C{\equiv}N)^-$ group.[43] According to Wang et al., the peaks at 2089 and 2126 cm^{-1} correspond to Fe^{2+}-CN-Mn^{2+} and Fe^{2+}-CN-Mn^{3+}, respectively.[34] The peak related to Fe^{3+}-CN-Mn^{2+} at round 2180 cm^{-1} is not observed, indicating that nearly all of the Fe in the compound remains as Fe^{2+}.[34] The PW-1 sample was also characterized by XPS to check the chemical states of Fe and Mn. As seen in Figure 1c,d, the bands at 707.8 and 720.8 eV can be assigned to $Fe^{2+}2p_{3/2}$ and $Fe^{2+}2p_{1/2}$, respectively.[44] The bands of Fe^{3+} are not present, indicating that the dominant Fe in the compound is divalent, agreeing with the Raman results. The XPS bands positioned at 641.4 and 653.4 eV are associated with $Mn^{2+}2p_{3/2}$ and $Mn^{2+}2p_{1/2}$, respectively, where a separation of the spin energy of 12 eV is observed.[45] The relatively broad band of the Mn 2p XPS suggests that trivalent Mn^{3+} is also present although main valence state of Mn is 2+.[44] The TG curves in Figure 1e show that the water content in PBAs is around 10%. The structural formulas of PW-1 and PW-2 were measured to be $Na_{1.80}Mn[Fe(CN)_6]_{0.98}\square_{0.02}{\cdot}1.76H_2O$ and $Na_{1.66}Mn[Fe(CN)_6]_{0.94}\square_{0.06}{\cdot}1.66H_2O$ ($\square$ = $Fe(CN)_6$ vacancy) by a combined ICP-AES and TG analyses along with the of C and N content measurements. The structural formula of the room-temperature sample was measured to be $Na_{1.79}Mn[Fe(CN)_6]_{0.87}\square_{0.13}{\cdot}1.69H_2O$. Although this sample contains a high sodium amount, it also contains a high $Fe(CN)_6$ vacancy. Namely, the sample prepared at low temperature is rich in defects, which can explain its relatively lower thermal stability (Figure S2b) compared with the high-temperature samples (Figure 1e).

The SEM images in Figure 2a,b show that, after adding sodium citrate in the $Na_4Fe(CN)_6$ solution, two shapes of particles are obtained, namely, small irregular and large cuboid particles. The particle size of the irregular product is about 200–600 nm, while the size of the cuboid particles is from 500 nm to several micrometers. For the PW-2 sample prepared without adding sodium citrate, it consists of submicron particles of about 200–600 nm. As a result, the average particle size can be increased by introducing sodium citrate with an increase in Na content. The increase in particle size may be favorable for easy electrode processing and reduced corrosion by electrolyte. TEM observation in Figure 2e,f confirms that PW-1 consists of irregular and cuboid particles while PW-2 consists of irregular particles. Figure 2g demonstrates HAADF-STEM images and energy dispersive X-ray spectrometry (EDX) mapping of a typical cuboid particle, which indicates the uniform element distribution. In comparison, EDX mapping of two small irregular particles suggests that the surface of the particles is Na deficient as shown in Figure 2h. The EDX mapping also shows that the Na content in the irregular particles is lower than that in the cuboid particles.

DOI: 10.1021/acssuschemeng.8b02758
ACS Sustainable Chem. Eng. 2018, 6, 16121–16129

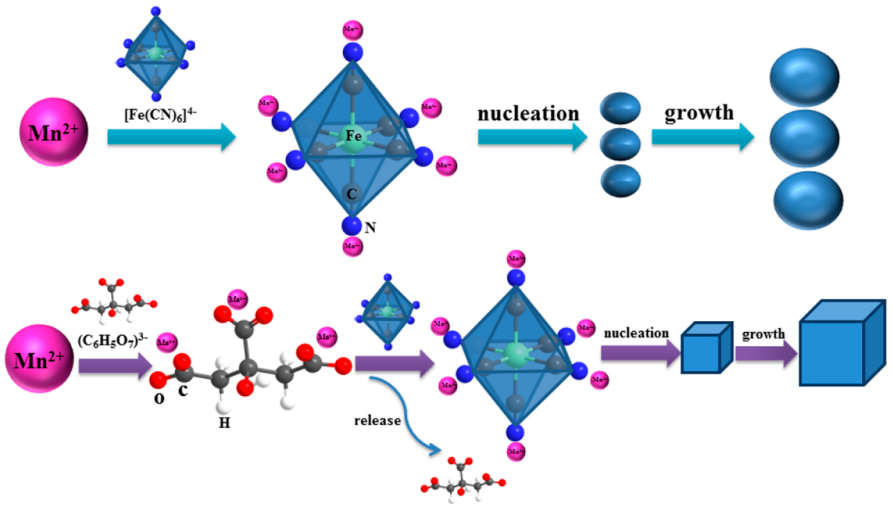

Figure 3. Schematic diagram of the formation mechanism of PW-1.

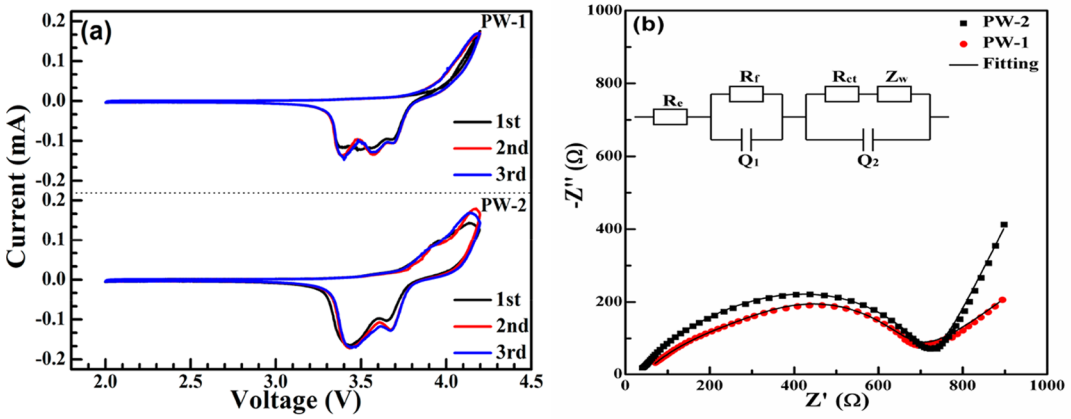

Figure 4. (a) CV and (b) EIS of PW-1 and PW-2.

Figure 3 illustrates the formation mechanism of PW-1. Without adding sodium citrate in the precursor solution, the PBA can nucleate and grow rapidly in the presence of sufficient Mn^{2+} and $[Fe(CN)_6]^{4-}$ ions. Therefore, numerous particles form with a small size and irregular shape. With the addition of sodium citrate, part of the Mn^{2+} ions can be absorbed by the sodium citrate to form complexes.[46] Therefore, two kinds of Mn^{2+} ions exist in the solution, namely, free and absorbed Mn^{2+} ions. During the reaction, the free Mn^{2+} ions can react rapidly with $[Fe(CN)_6]^{4-}$ ions to form irregular particles with a small size. In contrast, the low release rate of Mn^{2+} from the complexes leads to the slow nucleation and growth rate and therefore large particle size.[46] To verify the above assumption, a control experiment was performed where sodium citrate was added in the $MnSO_4$ solution side. As expected, all of the particles are cuboid shaped with a large size (Figure S3b). However, the product also has a monoclinic phase structure (Figure S3a). It can be concluded from the above results that the sodium citrate plays a critical role in the growth mode of PW.

Figure 4a exhibits the CV plots of PW-1 and PW-2 at a scan rate of 0.1 mV s^{-1}. Compared with that of PW-2, the oxidation peak of PW-1 slightly shifts to a higher voltage due possibly to large average particle size. PW-1 exhibits three successive reduction peaks between 3.4 and 3.8 V, while for PW-2, only two reduction peaks are observed. The difference in CV may arise from the different morphologies and compositions between the two samples. Figure 4b compares the EIS of PW-1 and PW-2. All of the plots consist of a flattened semicircle at high and middle frequency domain and an inclined straight line at low frequency domain. An equivalent circuit was used to fit the EIS plots. (inset in Figure 4b). The high-frequency intercept of the plots in Z' axis is associated with the ohmic resistance (R_e). The R_e includes the contact resistance between the particles, the interface resistance between electrolyte and current collector, and the electrolyte resistance. The flattened semicircle can be separated into two semicircles that associated with resistance for solid electrolyte interface (R_f) and resistance for charge transfer (R_{ct}) at electrode/electrolyte interface. The inclined line is related to the Warburg impedance for sodium-ions diffusion in the bulk material. The fitting data are listed in Table S2. From Table S2, we can see that, although PW-1 has a larger average particle size than PW-2, it has a somewhat lower R_{ct} value.

Figure 5a,b presents the charge/discharge curves of PW-1 and PW-2 at 0.1 C, where 1 C is defined as 150 mA g^{-1}. In the first cycle, PW-1 yields a charge capacity of 144.3 mAh g^{-1} and a discharge capacity of 144.0 mAh g^{-1} (Figure 5a), which agrees well with the theoretical value of PW-1 calculated from its structural formula. The large capacity is attributed to the large sodium content as discussed above. Moreover, the first Coulombic efficiency is as high as 99.8%, indicating rather high

DOI: 10.1021/acssuschemeng.8b02758
ACS Sustainable Chem. Eng. 2018, 6, 16121−16129

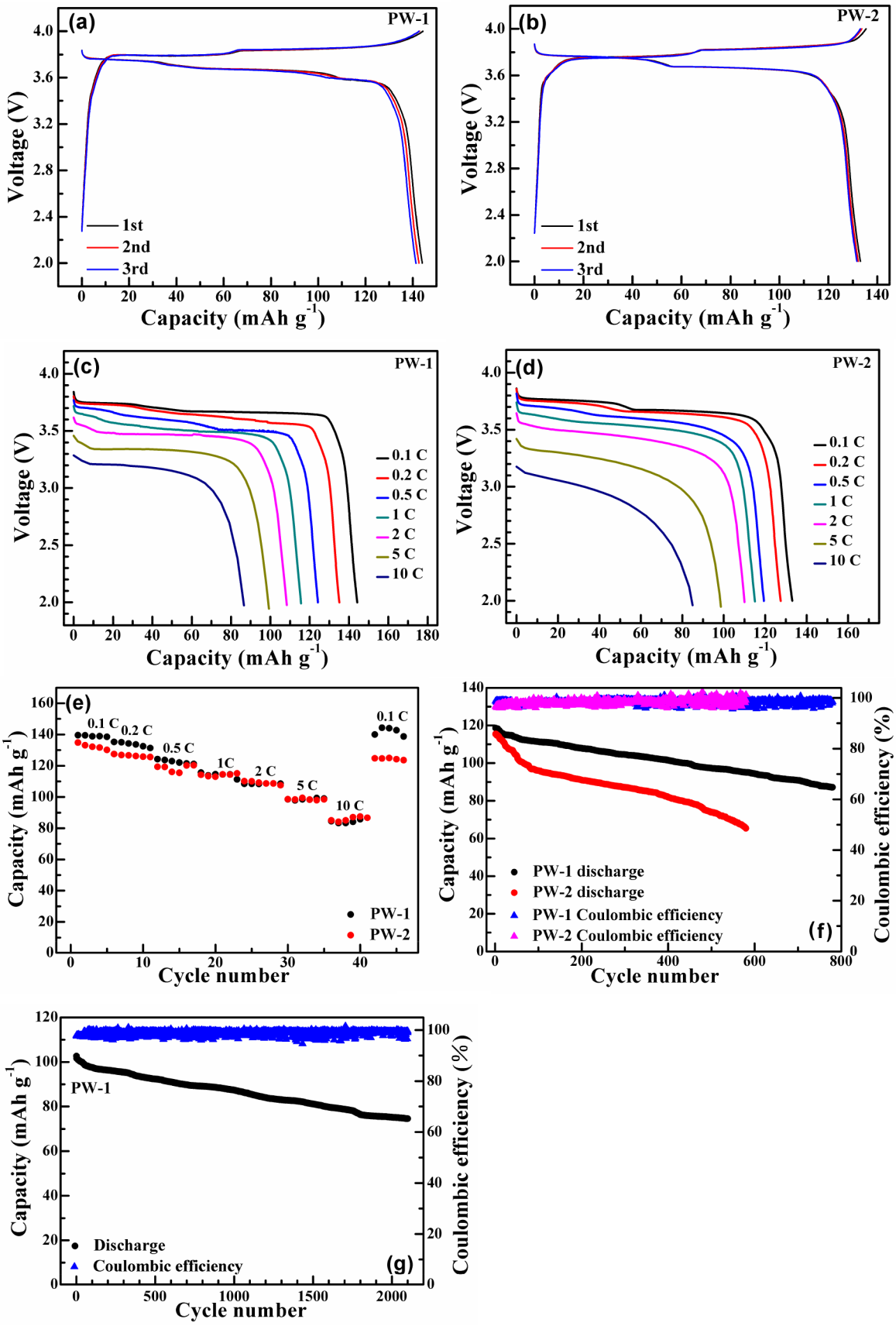

Figure 5. Charge/discharge curves of (a) PW-1 and (b) PW-2 under a 0.1 C rate, discharge curves of (c) PW-1 and (d) PW-2 under different rates with a charge current of 0.1 C, (e) the comparison of rate performance of PW-1 and PW-2, (f) the comparison of cycle life of PW-1 and PW-2 under a 0.5 C charge/discharge rate, and (g) cycle life of PW-1 under a 1 C charge/discharge rate.

DOI: 10.1021/acssuschemeng.8b02758
ACS Sustainable Chem. Eng. 2018, 6, 16121−16129

reversibility. In the first cycle, PW-2 delivers a charge capacity of 135.3 mAh g^{-1} and a discharge capacity of 133.1 mAh g^{-1}, corresponding to a 98.4% Coulombic efficiency. Obviously, PW-1 prepared by adding additive exhibits high capacity and Coulombic efficiency. For both PW-1 and PW-2, two successive potential plateaus can be observed, which are associated with redox couple of Fe^{2+}/Fe^{3+} and Mn^{2+}/Mn^{3+}, respectively.[34] For comparison, the electrochemical performance of the product prepared at room temperature was also tested (Figure S2c). In the first cycle, the product delivers a charge capacity of only 122.1 mAh g^{-1} and a discharge capacity of only 114.3 mAh g^{-1}. The low capacity is due to the defective crystal lattice when synthesized at low temperature as discussed above. Figure 5c,d presents the discharge profiles of PW-1 and PW-2 at various current densities, where the chare current density is fixed at 0.1 C (Figure S4). Note that PW-1 shows a similar discharge capacity as PW-2 at various current densities although the former has a larger average particle size than the latter. In addition, PW-1 has higher and more flat voltage plateau than PW-2, suggesting lower polarization and improved electrode kinetics which is favorable for practical applications. At 10 C, PW-1 still gives a relatively large discharge capacity of 86.6 mAh g^{-1}, which indicates good rate performance (Figure 5c,e).

Figure 5f compares cycling stability of PW-1 and PW-2 at 0.5 C. Obviously, PW-1 demonstrates enhanced cycling stability even though the two samples have similar initial capacity. PW-1 still keeps a high discharge capacity of 87.1 mAh g^{-1} after 780 cycles under a 0.5 C rate. For comparison, after 580 cycles, the discharge capacity of PW-2 fades quickly to 65.3 mAh g^{-1} at an identical current rate. The cycling performance of PW-1 was also studied under a 1 C rate (Figure 5g). After 2100 cycles under a 1 C rate, PW-1 still reserve a relatively large discharge capacity of 74.6 mAh g^{-1} with a 72.7% retention, indicating superior high-rate cycling stability. In comparison, the electrochemical performance of PW-3 was also tested (Figure S3c). Note that, although it also shows good cycling stability, the capacity is rather lower compared with that of PW-1. To clarify the excellent cycling performance of PW-1, the electrode after long-term cycling was observed using SEM (Figure 6). Of note is that both small irregular particles and large cuboid particles were corroded after 500 cycles as marked by the white arrows. As seen in Figure S5, small particles also suffer from corrosion (marked by white arrows), and even cracks appear during cycling (marked by black arrows). To highlight the outstanding cycling performance of our PW-1 sample, the electrochemical performance of some $Na_xMnFe(CN)_6$ materials is compared as summarized in Table S3. Clearly, the electrochemical performance of PW-1 is among the best.

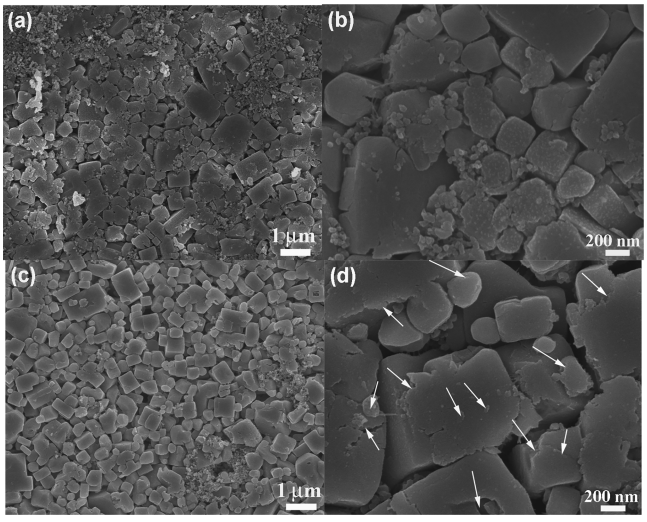

Figure 6. SEM images of (a,b) the original PW-1 and (c,d) the PW-1 electrodes after 500 cycles.

CONCLUSIONS

Prussia white material with superior performance was prepared by an improved precipitation method, where a surfactant sodium citrate was used to control the release rate of Mn^{2+} ions. The product (PW-1) with sodium citrate in precursor is composed is small irregular particles of 200−600 nm and large cuboid particles from 500 nm to several micrometers. In comparison, the size of the product (PW-2) without sodium citrate in the precursor is 200−600 nm. PW-1 (144.0 mAh g^{-1}) delivers a higher initial discharge capacity than PW-2 (133.1 mAh g^{-1}) due to its higher Na content. PW-1 shows comparable rate performance with PW-2 even though it has a large average particle size. In addition, PW-1 exhibits improved cycling performance compared with PW-2 with reduced corrosion by electrolyte because of large particle size. After 780 cycles under a 0.5 C rate, a large discharge capacity of 87.1 mAh g^{-1} is still maintained for PW-1. In comparison, the discharge capacity of PW-2 is reduced to 65.3 mAh g^{-1} after 580 cycles at an identical rate. After 2100 cycles under an 1 C rate, PW-1 could keep a relatively large discharge capacity of 74.6 mAh g^{-1} (72.7% remained). The outstanding electrochemical properties of the product make it a promising cathode for high-performance sodium-ion batteries.

ASSOCIATED CONTENT

Supporting Information

The Supporting Information is available free of charge on the ACS Publications website at DOI: 10.1021/acssuschemeng.8b02758.

XRD Rietveld refinement of PW-1; XRD, TG, and voltage profiles of the product prepared at room temperature; XRD, SEM, and cycling performance of PW-3 at a 1 C rate; discharge curves at different rates with a charge rate of 0.1 C of PW-1 and PW-2; SEM image of PW-2 after 500 cycles; fitting results for EIS; and comparison of electrochemical performance between Mn-based PBAs and the related references (PDF)

AUTHOR INFORMATION

Corresponding Author

*Tel./Fax: +86-571-87951451. E-mail: xiejian1977@zju.edu.cn.

ORCID

Jian Xie: 0000-0002-9376-5883

Notes

The authors declare no competing financial interest.

ACKNOWLEDGMENTS

This work was supported by the National Natural Science Foundation of China (No. 51572238), The Science and Technology Project of State Grid (No. SGRIDGKJ[2017]

DOI: 10.1021/acssuschemeng.8b02758
ACS Sustainable Chem. Eng. 2018, 6, 16121−16129

328), and the Strategic Emerging Industry Project of Hunan Province, China (2016GK4030).

REFERENCES

(1) Tarascon, J. M. Is Lithium the New Gold? *Nat. Chem.* **2010**, *2*, 510−510.
(2) Kubota, K.; Dahbi, M.; Hosaka, T.; Kumakura, S.; Komaba, S. Towards K-Ion and Na-Ion Batteries as "Beyond Li-Ion. *Chem. Rec.* **2018**, *18*, 459−479.
(3) Wang, Y. R.; Chen, R. P.; Chen, T.; Lv, H. L.; Zhu, G. Y.; Ma, L. B.; Wang, C. X.; Jin, Z.; Liu, J. Emerging Non-Lithium Ion Batteries. *Energy Storage Mater.* **2016**, *4*, 103−129.
(4) Choi, J. W.; Aurbach, D. Promise and Reality of Post-Lithium-Ion Batteries with High Energy Densities. *Nat. Rev. Mater.* **2016**, *1*, 16013.
(5) Pan, H. L.; Hu, Y. S.; Chen, L. Q. Room-Temperature Stationary Sodium-Ion Batteries for Large-Scale Electric Energy Storage. *Energy Environ. Sci.* **2013**, *6*, 2338−2360.
(6) Slater, M. D.; Kim, D.; Lee, E.; Johnson, C. S. Sodium-Ion batteries. *Adv. Funct. Mater.* **2013**, *23*, 947−958.
(7) Hong, S. Y.; Kim, Y.; Park, Y.; Choi, A.; Choi, N. S.; Lee, K. T. Charge Carriers in Rechargeable Batteries: Na Ions vs. Li Ions. *Energy Environ. Sci.* **2013**, *6*, 2067−2081.
(8) Kundu, D.; Talaie, E.; Duffort, V.; Nazar, L. F. The Emerging Chemistry of Sodium Ion Batteries for Electrochemical Energy Storage. *Angew. Chem., Int. Ed.* **2015**, *54*, 3431−3448.
(9) Hwang, J. Y.; Myung, S. T.; Sun, Y. K. Sodium-Ion Batteries: Present and Future. *Chem. Soc. Rev.* **2017**, *46*, 3529−3614.
(10) Fang, Y. J.; Chen, Z. X.; Ai, X. P.; Yang, H. X.; Cao, Y. L. Recent Developments in Cathode Materials for Na Ion Batteries. *Acta Phys.-Chim. Sin.* **2017**, *33*, 211−241.
(11) Fang, Y. J.; Chen, Z. X.; Xiao, L. F.; Ai, X. P.; Cao, Y. L.; Yang, H. X. Recent Progress in Iron-Based Electrode Materials for Grid-Scale Sodium-Ion Batteries. *Small* **2018**, *14*, 1703116.
(12) Fang, Y. J.; Xiao, L. F.; Chen, Z. X.; Ai, X. P.; Cao, Y. L.; Yang, H. X. Recent Advances in Sodium-Ion Battery Materials. *Electrochem. Energy Rev.* **2018**, *1*, 294−323.
(13) Xiang, X. D.; Zhang, K.; Chen, J. Recent Advances and Prospects of Cathode Materials for Sodium-Ion Batteries. *Adv. Mater.* **2015**, *27*, 5343−5364.
(14) Fang, C.; Huang, Y. H.; Zhang, W. X.; Han, J. T.; Deng, Z.; Cao, Y. L.; Yang, H. X. Routes to High Energy Cathodes of Sodium-Ion Batteries. *Adv. Energy Mater.* **2016**, *6*, 1501727.
(15) Kim, H.; Kim, H.; Ding, Z.; Lee, M. H.; Lim, K.; Yoon, G.; Kang, K. Recent Progress in Electrode Materials for Sodium-Ion Batteries. *Adv. Energy Mater.* **2016**, *6*, 1600943.
(16) Dai, Z. F.; Mani, U.; Tan, H. T.; Yan, Q. Y. Advanced Cathode Materials for Sodium-Ion Batteries: What Determines Our Choices? *Small Methods* **2017**, *1*, 1700098.
(17) Li, W. J.; Han, C.; Wang, W. L.; Gebert, F.; Chou, S. L.; Liu, H. K.; Zhang, X. H.; Dou, S. X. Commercial Prospects of Existing Cathode Materials for Sodium Ion Storage. *Adv. Energy Mater.* **2017**, *7*, 1700274.
(18) Moreau, P.; Guyomard, D.; Gaubicher, J.; Boucher, F. Structure and Stability of Sodium Intercalated Phases in Olivine $FePO_4$. *Chem. Mater.* **2010**, *22*, 4126−4128.
(19) Sathiya, M.; Hemalatha, K.; Ramesha, K.; Tarascon, J. M.; Prakash, A. S. Synthesis, Structure, and Electrochemical Properties of the Layered Sodium Insertion Cathode Material: $NaNi_{1/3}Mn_{1/3}Co_{1/3}O_2$. *Chem. Mater.* **2012**, *24*, 1846−1853.
(20) Liu, X. Z.; Wang, X.; Iyo, A.; Yu, H. J.; Li, D.; Zhou, H. S. High Stable Post-Spinel $NaMn_2O_4$ Cathode of Sodium Ion Battery. *J. Mater. Chem. A* **2014**, *2*, 14822−14826.
(21) Lu, Y. H.; Wang, L.; Cheng, J. G.; Goodenough, J. B. Prussian Blue: a New Framework of Electrode Materials for Sodium Batteries. *Chem. Commun.* **2012**, *48*, 6544−6546.
(22) Lee, H. W.; Wang, R. Y.; Pasta, M.; Lee, S. W.; Liu, N.; Cui, Y. Manganese Hexacyanomanganate Open Framework as a High-Capacity Positive Electrode Material for Sodium-Ion Batteries. *Nat. Commun.* **2014**, *5*, 5280.
(23) You, Y.; Wu, X. L.; Yin, Y. X.; Guo, Y. G. High-Quality Prussian Blue Crystals as Superior Cathode Materials for Room-Temperature Sodium-Ion Batteries. *Energy Environ. Sci.* **2014**, *7*, 1643−1647.
(24) Liu, Y.; Qiao, Y.; Zhang, W. X.; Li, Z.; Ji, X.; Miao, L.; Yuan, L. X.; Hu, X. L.; Huang, Y. H. Sodium Storage in Na-Rich $Na_xFeFe(CN)_6$ Nanocubes. *Nano Energy* **2015**, *12*, 386−393.
(25) Yang, D. Z.; Xu, J.; Liao, X. Z.; Wang, H.; He, Y. S.; Ma, Z. F. Prussian Blue without Coordinated Water as a Superior Cathode for Sodium-Ion Batteries. *Chem. Commun.* **2015**, *51*, 8181−8184.
(26) Chen, R. J.; Huang, Y. X.; Xie, M.; Zhang, Q. Y.; Zhang, X. X.; Li, L.; Wu, F. Preparation of Prussian Blue Submicron Particles with a Pore Structure by Two-Step Optimization for Na-Ion Battery Cathodes. *ACS Appl. Mater. Interfaces* **2016**, *8*, 16078−16086.
(27) Ren, W. H.; Qin, M. S.; Zhu, Z. X.; Yan, M. Y.; Li, Q.; Zhang, L.; Liu, D. N.; Mai, L. Q. Activation of Sodium Storage Sites in Prussian Blue Analogues via Surface Etching. *Nano Lett.* **2017**, *17*, 4713−4718.
(28) Yu, S. L.; Li, Y.; Lu, Y. H.; Xu, B.; Wang, Q. T.; Yan, M.; Jiang, Y. Z. A promising Cathode Material of Sodium Iron-Nickel Hexacyanoferrate for Sodium Ion Batteries. *J. Power Sources* **2015**, *275*, 45−49.
(29) Jiang, Y. Z.; Yu, S. L.; Wang, B. Q.; Li, Y.; Sun, W. P.; Lu, Y. H.; Yan, M.; Song, B.; Dou, S. X. Prussian Blue@C Composite as an Ultrahigh-Rate and Long-Life Sodium-Ion Battery Cathode. *Adv. Funct. Mater.* **2016**, *26*, 5315−5321.
(30) Wang, B. Q.; Han, Y.; Chen, Y. T.; Xu, Y. J.; Pan, H. G.; Sun, W. P.; Yan, M.; Jiang, Y. Z.; Liu, S. Gradient Substitution: an Intrinsic Strategy towards High Performance Sodium Storage in Prussian Blue-Based Cathodes. *J. Mater. Chem. A* **2018**, *6*, 8947−8954.
(31) Wang, B. Q.; Han, Y.; Wang, X.; Bahlawane, N.; Pan, H. G.; Yan, M.; Jiang, Y. Z. Prussian Blue Analogs for Rechargeable Batteries. *iScience* **2018**, *3*, 110−133.
(32) Qian, J. F.; Wu, C.; Cao, Y. L.; Ma, Z. F.; Huang, Y. H.; Ai, X. P.; Yang, H. X. Prussian Blue Cathode Materials for Sodium-Ion Batteries and Other Ion Batteries. *Adv. Energy Mater.* **2018**, *8*, 1870079.
(33) Wang, L.; Song, J.; Qiao, R. M.; Wray, L. A.; Hossain, M. A.; Chuang, Y. D.; Yang, W. L.; Lu, Y. H.; Evans, D.; Lee, J. J.; Vail, S.; Zhao, X.; Nishijima, M.; Kakimoto, S.; Goodenough, J. B. Rhombohedral Prussian White as Cathode for Rechargeable Sodium-Ion Batteries. *J. Am. Chem. Soc.* **2015**, *137*, 2548−2554.
(34) Wang, L.; Lu, Y. H.; Liu, J.; Xu, M. W.; Cheng, J. G.; Zhang, D. W.; Goodenough, J. B. A Superior Low-Cost Cathode for a Na-Ion Battery. *Angew. Chem., Int. Ed.* **2013**, *52*, 1964−1967.
(35) Wu, X. Y.; Wu, C. H.; Wei, C. X.; Hu, L.; Qian, J. F.; Cao, Y. L.; Ai, X. P.; Wang, J. L.; Yang, H. X. Highly Crystallized $Na_2CoFe(CN)_6$ with Suppressed Lattice Defects as Superior Cathode Material for Sodium-Ion Batteries. *ACS Appl. Mater. Interfaces* **2016**, *8*, 5393−5399.
(36) Song, J.; Wang, L.; Lu, Y. H.; Liu, J.; Guo, B. K.; Xiao, P. H.; Lee, J. J.; Yang, X. Q.; Henkelman, G.; Goodenough, J. B. Removal of Interstitial H_2O in Hexacyanometallates for a Superior Cathode of a Sodium-Ion Battery. *J. Am. Chem. Soc.* **2015**, *137*, 2658−2664.
(37) Yang, D. Z.; Xu, J.; Liao, X. Z.; He, Y. S.; Liu, H. M.; Ma, Z. F. Structure Optimization of Prussian Blue Analogue Cathode Materials for Advanced Sodium Ion Batteries. *Chem. Commun.* **2014**, *50*, 13377−13380.
(38) Li, W. J.; Chou, S. L.; Wang, J. Z.; Wang, J. L.; Gu, Q. F.; Liu, H. K.; Dou, S. X. Multifunctional Conducing Polymer Coated $Na_{1+x}MnFe(CN)_6$ Cathode for Sodium-Ion Batteries with Superior Performance via a Facile and One-Step Chemistry Approach. *Nano Energy* **2015**, *13*, 200−207.
(39) You, Y.; Yao, H. R.; Xin, S.; Yin, Y. X.; Zuo, T. T.; Yang, C. P.; Guo, Y. G.; Cui, Y.; Wan, L. J.; Goodenough, J. B. Subzero-Temperature Cathode for a Sodium-Ion Battery. *Adv. Mater.* **2016**, *28*, 7243−7248.

DOI: 10.1021/acssuschemeng.8b02758
ACS Sustainable Chem. Eng. 2018, 6, 16121−16129

(40) Huang, Y. X.; Xie, M.; Zhang, J. T.; Wang, Z. H.; Jiang, Y.; Xiao, G. H.; Li, S. J.; Li, L.; Wu, F.; Chen, R. J. A Novel Border-Rich Prussian Blue Synthesized by Inhibitor Control as Cathode for Sodium Ion Batteries. *Nano Energy* **2017**, *39*, 273−283.
(41) Jo, I. H.; Lee, S. M.; Kim, H. S.; Jin, B. S. Electrochemical Properties of $Na_xMnFe(CN)_6 \cdot zH_2O$ Synthesized in a Taylor-Couette Reactor as a Na-Ion Battery Cathode Material. *J. Alloys Compd.* **2017**, *729*, 590−596.
(42) Peng, J.; Wang, J. S.; Yi, H. C.; Hu, W. J.; Yu, Y. H.; Yin, J. W.; Shen, Y.; Liu, Y.; Luo, J. H.; Xu, Y.; Wei, P.; Li, Y. Y.; Jin, Y.; Ding, Y.; Miao, L.; Jiang, J. J.; Han, J. T.; Huang, Y. H. A Dual-Insertion Type Sodium-Ion Full Cell Based on High-Quality Ternary-Metal Prussian Blue Analogs. *Adv. Energy Mater.* **2018**, *8*, 1702856.
(43) Vertelman, E. J. M.; Lummen, T. T. A.; Meetsma, A.; Bouwkamp, M. W.; Molnar, G.; van Loosdrecht, P. H. M.; van Koningsbruggen, P. J. Light- and Temperature-Induced Electron Transfer in Single Crystals of $RbMn[Fe(CN)_6] \cdot H_2O$. *Chem. Mater.* **2008**, *20*, 1236−1238.
(44) Huang, Y. X.; Xie, M.; Wang, Z. H.; Jiang, Y.; Yao, Y.; Li, S. J.; Li, Z. H.; Li, L.; Wu, F.; Chen, R. J. A Chemical Precipitation Method Preparing Hollow-Core-Shell Heterostructures Based on the Prussian Blue Analogs as Cathode for Sodium-Ion Batteries. *Small* **2018**, *14*, 1801246.
(45) Liu, Y.; He, D. D.; Han, R. M.; Wei, G. Y.; Qiao, Y. Nanostructured Potassium and Sodium Ion Incorporated Prussian Blue Frameworks as Cathode Materials for Sodium-Ion Batteries. *Chem. Commun.* **2017**, *53*, 5569−5572.
(46) Chen, R. J.; Huang, Y. X.; Xie, M.; Wang, Z. H.; Ye, Y. S.; Li, L.; Wu, F. Chemical Inhibition Method to Synthesize Highly Crystalline Prussian Blue Analogs for Sodium-Ion Battery Cathodes. *ACS Appl. Mater. Interfaces* **2016**, *8*, 31669−31676.

DOI: 10.1021/acssuschemeng.8b02758
ACS Sustainable Chem. Eng. 2018, 6, 16121−16129